

High Redshift Supernovae in the Hubble Deep Field¹

Ronald L. Gilliland², Peter E. Nugent³, M. M. Phillips⁴

Received _____; accepted _____

¹Based on observations with the NASA/ESA *Hubble Space Telescope*, obtained at the Space Telescope Science Institute, which is operated by AURA, Inc., under NASA contract NAS 5-26555.

²Space Telescope Science Institute, 3700 San Martin Drive, Baltimore, MD 21218; gillil@stsci.edu

³E.O. Lawrence Berkeley National Laboratory, 1 Cyclotron Road, MS 50-232, Berkeley, CA 94720; penugent@lbl.gov

⁴Carnegie Institution of Washington, Las Campanas Observatory, Casilla 601, La Serena, Chile; mmp@ociw.edu

ABSTRACT

Two supernovae detected in the Hubble Deep Field (HDF) using the original December 1995 epoch and data from a shorter (63000 s in F814W) December 1997 visit with *HST* are discussed. The supernovae (SNe) are both associated with distinct galaxies at redshifts of 0.95 (spectroscopic) from Cohen et al. (1996) and 1.32 (photometric) from the work of Fernández-Soto, Lanzetta, & Yahil (1998). These redshifts are near, in the case of 0.95, and well beyond for 1.32 the greatest distance reported previously for SNe. We show that our observations are sensitive to supernovae to $z \lesssim 1.8$ in either epoch for an event near peak brightness. Detailed simulations are discussed that quantify the level at which false events from our search phase would start to arise, and the completeness of our search as a function of both SN brightness and host galaxy redshift. The number of Type Ia and Type II SNe expected as a function of redshift in the two HDF epochs are discussed in relation to several published predictions and our own detailed calculations. A mean detection frequency of one SN per epoch for the small HDF area is consistent with expectations from current theory.

Subject headings: stars: supernovae — cosmology: general — cosmology: observations — methods: numerical

1. Introduction

Supernovae provide sensitive probes for conditions in the early universe. Type II supernovae (SNe II) events arising from final gravitational collapse and rebound in massive stars reflect the star formation rate (SFR) with essentially no lag time for the high end of the initial mass function (IMF) and their detection may allow quantification of the SFR even in galaxies which are too faint for direct imaging. Type Ia supernovae (SNe Ia) are the brightest supernovae (with luminous Type Ic events also at the top end of brightness distributions) and are established as standard candles on both theoretical and observational grounds. The extent to which Type Ia SNe deviate from being perfect standard candles in terms of intrinsic magnitude scatter following corrections from decline rate and spectral intensity distribution correlations, as well as possible systematics with look back time remain topics of vigorous investigation. SNe Ia are thought to arise from thermonuclear runaways in White Dwarfs (WDs) passing the Chandrasekhar mass limit as a result of either double degenerate mergers or mass transfer and accretion in a close binary system. The SN Ia rates are therefore less directly connected to the SFR than for SNe II, but nonetheless with a lag necessary to first form WDs via stellar evolution, then time for the WD to grow in mass, their rates will reflect the rate of star formation in the early universe.

Supernovae are also responsible to first order for the overall chemical evolution of the Universe. SNe II are the primary source of metals below the Iron peak and provide early heavy element creation from the most massive stars. SNe Ia are thought to provide the primary source of Iron peak elements. The relative frequency of these SNe types (SNe II coming first followed by a later relative increase in the SN Ia rates) can therefore explain in a simple way the overall increase of metals with time in an evolving universe, and also account for the relative overabundance of Oxygen to Iron seen in the early universe and old stellar populations.

The detection and study of SNe are of obvious importance both for their utility as cosmological probes, and also for their fundamental role in determining chemical evolution. Using specially crafted, two-epoch, ground-based searches (e.g., Perlmutter et al. (1999); Schmidt et al. (1998)) many SN Ia events are now routinely detected near $z \sim 0.5$, and a few to $z \sim 1.0$ (Garnavich et al. (1998)) and even beyond have been found (Aldering et al., 1998). Using SNe Ia as standard candles yields a cosmology with low matter density and a non-zero cosmological constant (Perlmutter et al., 1999; Riess et al., 1998).

SNe Ia near maximum light have a flux maximum near 400-500 nm and a steep flux decline below about 260 nm (Kirshner et al., 1993). Programs designed for efficient detection of distant SNe are constrained to redshifts of $1+z \sim \text{filter center wavelength}/260$ nm. For the longest wavelength filter, F814W, used for the HDF this corresponds to $z \sim 2.0$, the effective limit of our two-epoch SN search. At $z \sim 1.7$ a normal SN Ia will have a peak I - band (we will use Johnson-Cousins magnitudes throughout) magnitude of $m_I \sim 26.5$ which is already beyond the detection limit based on point spread function shape alone (Flynn, Gould, & Bahcall (1996)) that point source versus diffuse object discrimination can be made for even the uniquely deep HDF. Detection and detailed study of SNe Ia through their first occurrence (perhaps $z \sim 3-4$ given a reasonable delay time from the Big Bang) in the early universe is one of the key drivers for the Next Generation Space Telescope (NGST) planning (Madau, Valle, & Panagia (1998)). Our WFPC2-*HST* search uses the existing F814W deep image of the HDF and an additional (less) deep F814W HDF image two years later providing two independent epochs in which SNe can be searched for. The project goal is to quantify the utility of *HST* for conducting searches for cosmological SNe and to return information on the SN rate to $z \sim 2$ in the early universe. Since this initial project does not allow for obtaining verification spectra to classify individual events by type, nor is a substantial time base during either epoch of observation available to define a light curve, quantitative application to testing cosmology parameters is not expected.

The observations of the original HDF and our second epoch imaging will be briefly reviewed in §2. Since our data reductions differ from those used for the standard HDF releases (Williams et al., 1996), discussion is provided in §3 to document these basics. The SN detected in the HDF will be discussed in detail in §4 along with quantification of completeness limits and false signal occurrence. Detectability of SNe with redshift, given our data characteristics and intrinsic properties of SNe Ia and SNe II is developed in §5 along with a comparison with several recent theoretical predictions. Discussion of cosmological and more mundane implications is given in the §6 summary.

2. Observations

With goals of pushing *HST* capabilities (pre-NICMOS for this Cycle 6 program) for detection of high- z SN, and detecting a few events with concomitant implications for SN rates at high z we obtained second epoch observations of the HDF in the F814W filter. Although the F606W HDF images are intrinsically deeper, F814W provides a greater sensitivity for high- z SN events nearly in proportion to the relative filter wavelengths as a result of the steep drop off in UV flux (this has been shown with detailed K-correction evaluations). SNe will be detected as point-like sources that are visible in either, but not both epochs.

To maximize mutual areal coverage, and to minimize problems with image differences across epochs for these under-sampled data, the second epoch data were obtained at an *HST* orient as closely matching the original as possible.

In order to obtain critical sampling for the WF pixel size of $0''.1$ with inherently undersampled data the original epoch F814W exposures were dithered to 10 sub-pixel pointings (9 by design, one extra as a result of a guide star acquisition problem in one visit).

The sub-pixel offsets were linked with large scale offsets over $\sim \pm 2''$ to help in averaging out spatial imperfections in the CCD response. At each dither position 4 to 6 exposures were taken and then cosmic rays were eliminated as multi-sigma deviations across these short stacks (in the standard reductions described in Williams et al. (1996)) at common pointings.

A constraint of this SN program is to not only detect objects to well quantified completeness limits, but to do so with an assurance that **no** false events from either noise fluctuations (Poisson, cosmic rays) or CCD defects such as hot pixels are included. Robust image subtractions require excellent sampling implying a need for at least as many sub-pixel dithers in the second epoch observations as in the original. Robust control against hot pixels (in undersampled data a hot pixel is difficult to distinguish from a faint point source, and over the course of these observations many new hot pixels are created) argues for a large number of dithers to independent pixels. For these second epoch observations (18 orbits in the continuous viewing zone) one independent dither offset per orbit was used. In order to keep readout noise well below sky only two F814W exposures (1600s, 1900s) were taken per orbit, thus only two (or in the case of F300W exposures taken during the bright phase of each orbit, one) exposures at any one pointing. Although for many projects cosmic ray elimination using pairs of exposures would be acceptable, it would be a disaster for this project since many spurious signals would arise from chance coincidence of cosmic rays across image pairs. We therefore required code capable of eliminating cosmic rays across the full image stacks simultaneously, even if all of the exposures had unique pointings.

Table 1 summarizes the original epoch F814W data and the second epoch F814W and F300W data. The F300W images are used as darks to define hot pixels for the purposes of these observations, and extend the archival data base. The F300W images do not have a magnitude limit useful for constraints on high-z SNe. The second epoch for F814W was

731.9 days after the first, or 2.00 years. For both epochs the F814W data was acquired in generally dark, and nearly equal conditions (only $\sim 20\%$ of frames show any evidence of scattered light). During the original epoch a subset of 4 frames had a $4.5'$ rotation with respect to the others; all of the second epoch data was rotated by $8.8'$ with respect to the bulk of the original. Total exposure time in the second epoch F814W data is 51% of that obtained in the original HDF.

EDITOR: PLACE TABLE 1 HERE.

3. Data Reductions

For the data reductions described in this section the following goals apply: (1) Derive an over-sampled, summed image for each epoch of F814W data. (2) Use optimal weights to minimize background noise. (3) Use precise knowledge of relative frame-to-frame offsets and an algorithm that provides sharp, clean point spread functions. (4) Eliminate both cosmic rays and hot pixels such that any residual signals from these are well below claimed SN detection levels. (5) Correct for the WFPC2 scattered light pattern in any affected frames. (6) Construct the second epoch image on exactly the same sky-reference grid as defined by external galaxies as was used for the first epoch solution. (7) Provide an error array for each epoch that accurately reflects relative errors. Successfully reaching these goals will enable SN searches by simply taking differences of the two epoch images and searching for point-like sources at several sigma above the expected background fluctuations.

Several of the data reduction steps discussed next are not independent, for example derivation of an image model and good cosmic ray rejection requires knowledge of the image registration, and an accurate derivation of the image registrations requires prior knowledge of the “true” image and good cosmic ray elimination. Fortunately the process is convergent,

adopting a decent guess for the image registrations (from the commanded dithers, or from “off-line” measurement of a few primary sources) provides sufficient accuracy for a first round of image model creation and cosmic ray elimination. The initial image model then supports improved derivation of relative registrations.

The reduction steps discussed below all start with the pipeline calibrated images (for the original epoch the recalibrations as discussed in Williams et al. (1996)). We start by rotating data for each CCD by multiples of 90 degrees to align on the sky with WF4. In this initial step the data are also scaled to e- by multiplying by the gain (~ 7 e-/DN) for each CCD, the resulting images are stored as i*2 data to save storage (no degradation of signal to noise results from this step). A global sky level is evaluated for each frame as the first moment position of a histogram within 3σ of the peak generated from the central 600×600 pixels for each frame, this global value is then subtracted from each image.

3.1. Image Model and Cosmic Ray Rejection

Elimination of cosmic rays from Wide Field Camera data containing stellar images and for which even minor frame-to-frame offsets exist is problematic (most of the HDF area is rather easier to deal with since most structures are slowly varying at the pixel scale). The sharp PSFs lead to variations at a given pixel of recorded flux near stellar cores that vary by a full factor of 10 with relative dithers of one pixel. In order to retain full sensitivity to detecting cosmic rays at a few sigma above a pixel’s expected noise level requires knowledge of how the intrinsic intensity changes for a given pixel correlate with the relative change of pixel to sky mapping frame-to-frame: this is the definition of image model (see discussion in Gilliland et al. (1995)).

Given a series of independent images in time with sub-pixel offsets frame-to-frame of

$\delta x_{i,j}(t)$, $\delta y_{i,j}(t)$ the image model is:

$$I_{i,j}(t) = f[\delta x_{i,j}(t), \delta y_{i,j}(t)] \quad (1)$$

where the function f is chosen to have enough variation to match the rapid change of $I_{i,j}$ experienced in under-sampled data. We have used up to a third-order polynomial (10 terms) in both x and y to yield a good model intensity. In this approach the expected CCD image of the sky at any arbitrary sub-pixel offset, as sampled by the broad CCD pixels, can be calculated as a function of the relative sub-pixel (integer shifts are factored out of this representation) x , y offset. It is then a simple matter to flag and eliminate cosmic rays as multi-sigma deviations (we use 3 standard deviations in a primary search step, then allow “growth” of cosmic rays by lowering the threshold to 1.8σ for pixels within a radius of one pixel) of individual data points from this image model.

This image model then serves multiple purposes: (1) allows full sensitivity to cosmic ray detection in under-sampled and dithered data, (2) supports image registration determination (§3.2), (3) supports scattered light removal (§3.3), (4) and can be used to create an over-sampled image simply by evaluating Eq. (1) at a number of regular sub-pixel coordinates (but see §3.5, a different approach is adopted here for generating a combined image in support of the SN search).

The image model is developed by fitting the polynomial representation of Eq. 1 to a stack of pixel values corresponding to the separately known x , y offsets with weights given as the inverse variance expected from Poisson noise on the object and sky plus readout noise. For pixels on the inner wings of bright stars the full 10 parameter representation is required for a good match of model and data. In regions dominated only by sky background such a multi-parameter fit is inappropriate and over-fits the data, producing an excessively noisy background if used to produce an over-sampled image. To avoid the latter problem

the number of terms allowed in the image model fit for any pixel is adjusted as a function of mean signal level. Also, given the relatively small number of sub-pixel dithers, coupled with geometric distortion some pixels will have good phase-space coverage in the offsets and others will have a very unbalanced distribution of sub-pixel x, y sampling – this is also taken into account in determining how many terms are used to represent Eq. 1 for any pixel. The net result of this is a *variable resolution* model of the spatial distribution of light on the sky: high resolution near bright objects, low in regions of low signal (or inherently poor dither sampling at the sub-pixel level). The variable resolution is appropriate for supporting cosmic ray detection and image registration, but quite inappropriate for a final mean image for which underlying PSF stability is needed in support of object detection and characterization.

3.2. Image Registration.

Since we wish to derive combined images with over-sampling to optimally recover critical sampling, accurate knowledge of frame-to-frame offsets is essential. Fortunately, even in the sparse HDF and low-signal F300W images there is adequate information in compact objects to support such relative offset determination.

Geometric distortion exists in the WFPC2 cameras at a sufficient level that it must be directly accounted for in developing the offsets for any pixel. We have used a simple r^3 distortion term with separate centers and coefficients determined for each CCD camera as necessary to bring images at the edges of adjacent chips (provided by the K-spot calibration images) into registration. Inspection of distortion maps as provided in Holtzman et al. (1995) shows that such a simple radial term is appropriate and our three parameter (x, y center for each chip and coefficient on the cubic term) representation provides accurate results and is much easier to work with than the twenty-term, two-dimensional polynomials.

For these analyses we correct for geometric distortion only in a differential sense, our final combined images retain the intrinsic WFPC2 distortion, but the effect of geometric distortion in producing variable offsets as a function of position over the CCD in response to large dithers is fully accounted for.

A further complication in both the original and second epoch data are small rotations (up to 0.0025 radians) sufficient to generate relative shears of one pixel in the CCD corners if not accounted for. Across epochs we also cannot assume that the plate scale remains constant to the accuracy we need ($\lesssim 0.1$ pixel side-to-side on a CCD).

The image registration therefore accounts for: (1) x, y offsets at chip center are evaluated for every frame. (2) Geometric distortion is modeled to yield correct sub-pixel offsets for all individual pixels as a function of their position in CCD coordinates and the primary offsets. (3) A simple rotation matrix adjustment of x, y offsets away from chip center. The rotation may be assumed constant for all of the second epoch relative to the first, constant at a different value for the four images affected within the first epoch, and the values derived from the high S/N F814W data may be assumed for the F300W images. (4) A separate x and y plate scale for each CCD camera to be evaluated only as the second epoch relative to the first. A formal solution yielded a plate scale difference of $\sim 8 \times 10^{-5}$ in the x direction (all chips rotated to align with WF4), and half this in the y direction across the epochs. This yields a relative shift of 0.06 pixels side-to-side over the CCDs. Independent determinations for the three WF chips showed a scatter of $\pm 15\%$. In generating combined images for the second epoch we have accounted for this marginally significant, albeit relatively unimportant term.

The image model provided by Eq. 1 consists of CCD-sized arrays for each of the 10 polynomial coefficients. As previously discussed only a subset of the coefficients are used (down to just the zero point in regions of sky background) based on local data

characteristics. Furthermore during the solution for Eq. 1 on each pixel, terms are only retained if judged significant (magnitude greater than twice the error). The pixel-by-pixel solution is iteratively developed retaining only significant terms (e.g., on the edge of a bright star all 10 terms would likely be kept, on sky only the zero point, and in the center of a bright, but broad galaxy only the zero point). The image model therefore very directly reflects which pixels (those with both a substantial signal level and several populated higher order terms) carry significant positional information. For a given CCD we utilize the $\sim 1\%$ of pixels carrying almost 100% of the positional information in evaluating registration offsets.

We compute image registration offsets (and sometimes rotations and/or plate scale changes) for individual frames by evaluating what offsets yield the optimal (in a weighted least-squares sense) match of the evaluated image model (Eq. 1) “shifted” to register with individual frames. Only the relatively noiseless model image is evaluated with different shifts and this process does not involve interpolation of individual under-sampled images. After the first iteration of this process the individual images have been cleaned of cosmic rays (pixels flagged as having been hit by a cosmic ray have had data values replaced by the image model value). Resulting image registrations for individual F814W images are good to ~ 0.02 pixels for the basic x, y offsets and to $\lesssim 0.05$ pixels side-to-side for rotation and/or plate scale change effects.

The above approach works very well when applied to individual frames in the original epoch in reference to the model image of the original. Since we will search for SNe in difference images across the two epochs, and thus need excellent registration of the two, we also register individual frames of the second epoch against the model image from the first. In our first full solution it became immediately obvious that the two epoch difference image showed poor subtractions of both stars and galaxies. Near the position of bright stars

the difference images tended to show negative to positive intensity gradients in random directions – stars move; proper motion over two years was sufficient to generate significant registration differences for stellar sources. We then dropped all stars detected by Flynn *et al.* 1996 from the cross-epoch registration solution and immediately obtained excellent subtractions on galaxies. (Stars fainter than the Flynn sample are at too low a signal to noise to influence the registrations.)

3.3. Scattered Light Removal

The WFPC2 cameras generate characteristic (but variable according to details of illumination) large scale “X” patterns of excess background light from bright Earth limb photons directed into the *HST* optical truss at shallow angles. Since added light carries a Poisson noise penalty, even if the pattern can be subtracted out, the best approach to scattered light is to avoid observing close to the bright Earth limb. However, with the availability of Continuous Viewing Zone observations and wanting to use as much of each orbit as possible, it is likely that a subset of the images will show low levels of scattered light.

We define and correct for scattered light via the following approach: (1) Using a subset of exposures entirely free of scattered light define a model image as in §3.1. (2) Use the scattered light free image model and subtract it on a frame-by-frame basis from all images with possible scattered light contamination. This is done on images that have been cleaned of cosmic rays. (3) Smooth the resulting images using Fourier filtering and subtract the resulting images from the individual data arrays before performing a final combination. This approach works well and provides a final combined image with no trace of the scattered light pattern.

3.4. Delta-Dark and Hot Pixel Definition

Scaled to a typical exposure time (2700s) of individual input frames the final combined HDF F814W images should have an rms noise in regions of sky of ~ 1.85 e- and 2.65 e- for the first and second epochs respectively, or 3.23 e- for the difference image. Any “hot” pixels with count rates $\gtrsim 3.23/2700 = 0.0012$ e-/s, or on average less than 1 DN (at a gain of 7 e-/DN) per integration will thus contribute equally to the final noise (or start to rise above it and thus mimic an event). The darks can be determined to a level several times better than this ($\sim 2.2 \times 10^{-4}$ e-/s rms first epoch, and $\sim 3.8 \times 10^{-4}$ e-/s for the second epoch; for the longest exposure times in both epochs this corresponds to 0.7 e- rms uncertainty in the dark contribution for typical pixels per readout) as we argue next.

The HDF data using multiple available bandpasses and augmented with any contemporaneous real dark exposures can be used very effectively to define a delta-dark (a primary dark image has been removed already in the pipeline reductions for each frame) and to search for any hot pixels, including especially those that only become hot during the interval of the observations. Using image models as defined in §3.1 we create individual frames that have been: (1) through standard pipeline reductions, (2) cleaned of cosmic rays, but with retention of cosmic ray images (i.e., the spatial distribution of light attributed to cosmic rays on a frame-by-frame basis), (3) cleaned of any scattered light, and (4) subtracted using the image model (i.e., the real sources are removed). The resulting images should simply be random noise (sky and object Poisson plus readout), plus any dark not yet accounted for. These resulting images are all scaled to a common exposure time and stacked in direct pixel space. (To search for hot pixels with large amplitude the cosmic rays must be added back in, since at least in the second epoch data the frequent dithering would result in their elimination as cosmic rays.) A consistently hot pixel will stand out as having a positive value throughout and fluctuations as expected from Poisson and readout noise.

For each pixel a sample mean is formed for values within the 10th and 90th percentiles using appropriate weights from each individual pixel-frame (a pixel that was sitting on a bright target in a given frame would have a low weight due to Poisson noise). This becomes a new delta-dark image. All pixel time series are checked for a number of anomalies and if any of the following tests “succeed” then the pixel is flagged as bad and not used in forming a final combined image: (1) absolute value of the dark rate exceeds 0.008 e-/s, (2) the standard deviation on the pixel time series is more than 1.5 times the expected value, (3) the absolute value of difference between the first 10% (in time) and last 10% ratioed to the overall standard deviation exceeds 3.5 (these are pixels that turned on or off during the observing period), (4) a linear correlation coefficient between pixel values and local sky level exceeds 0.25 (evidence of a low amplitude non-linearity or trap).

The second epoch data used to define darks included 76 F814W, F300W and dark images totaling a dark accumulation time (slightly longer than exposure time) of 122,160 s on WF2. The original epoch data used included 157 F814W, F300W and F450W images totaling 374,100 s. (Darks had not been reduced using the same master dark as the data frames; since the available data was more than sufficient already the first epoch dark frames were not brought in. Images with either short exposure times, or excessive sky levels were dropped.)

Summed over the four CCDs 2222 pixels were already flagged as bad by the pipeline (we keep these flagged as bad), after augmentation by the above tests we carry an additional 15,465 bad pixels (second epoch, similar size, but different list in first) – still only 0.8% of all pixels in active imaging areas. The remaining >99% of pixels with delta-dark rates ≤ 0.008 e-/s are then additionally corrected for these (appropriately scaled dark integration time) delta-dark values. Our combined images (next section) have marginally better (averages 2.1% for the three WF chips in F814W) levels of background noise in comparison with the

Version 2 HDF release (Williams *et al.* 1996) and significantly better at 21.8% for the single case (PC1 and F300W) most sensitive to having details of the dark current and elimination of slightly bad pixels done optimally.

We have been particularly diligent in defining (and then ignoring) hot pixels, since for SN detection in undersampled data a hot pixel at ~ 0.035 e-/s provides the same count level as a SN of $m_I \sim 27.3$ near our detection limit.

3.5. Image Combination

We have already described in §3.1 an image model that provides one realization of image combination algorithms. However, its over-fitting of noise in regions of low signal, or resolution dependence on local signal if the fit order is varied makes this a poor realization in which to search for faint point sources. (This technique is ideal for use as an intermediate tool for eliminating cosmic rays, deriving image registrations, etc.)

In support of SN detection a combined image for each epoch that retains all available spatial information, maintains photometric stability and reaches the noise floor specified by simple Poisson statistics and readout noise is desired. A strong candidate for providing this was the “drizzle” software used in the original release of combined HDF images. A minor weakness noted in Williams *et al.* 1996 for the drizzle approach was that PSFs on the brighter stars showed “noticeable high-frequency noise” (seen even in simulations without Poisson noise). We have chosen a more “continuous” approach to assigning values on an over-sampled grid, than the discrete apportionment of flux from individual WF pixels used by drizzle; in principle this should produce a more stable PSF. In practice our approach does seem to provide a slightly sharper and smoother PSF than was realized in the Version 2 drizzle results, although real gains are marginal at best at a level of a few percent.

Our algorithm is even simpler than drizzle and consists of the following: (1) Start with a stack of frames for which all available corrections (calibration reductions for bias, flat-field and dark; sky and scattered light subtracted; a delta-dark subtracted) have been made and for which frame-to-frame registration is accurately known as well as knowledge of all pixels affected by cosmic rays. (2) Define a regular grid of over-sampled positions in pixel space (or on the sky if geometric distortion removal in this step is desired) upon which the combined image will be defined. We use a regular grid of $\times 4$ over-sampled sub-pixels, the resulting image retains geometric distortion. (3) Adopt a weighting function to transfer values from pixels with arbitrary, nearby offsets to an accumulation at the grid positions.

We use a simple Gaussian weighting with a width parameter of ~ 0.3 WF pixels. The intensity at an arbitrary x, y grid position is:

$$I_{xy} = \frac{\sum_{i=1}^I \sum_{j=1}^J \sum_{n=1}^N gw_{i,j,n} pw_{i,j,n} I_{i,j,n}}{\sum_{i=1}^I \sum_{j=1}^J \sum_{n=1}^N gw_{i,j,n} pw_{i,j,n}} \quad (2)$$

where the Gaussian weighting is specified as:

$$gw_{i,j,n} = e^{-\left(\frac{(x_{i,j,n} - x)^2 + (y_{i,j,n} - y)^2}{\sigma^2}\right)} \quad (3)$$

and the $pw_{i,j,n}$ are pixel weights set as the inverse variance sum of Poisson and readout noise components. The $x_{i,j,n}$ and $y_{i,j,n}$ are the relative offsets of a given pixel accounting for geometric distortion, the frame-to-reference image registration offsets, rotation and plate scale changes. The range of n is over the full stack of images (58 F814W in first epoch, 36 for second), and in principle i and j range over the full indices on each frame, but the Gaussian cut off is steep enough that in practice only pixels within ± 1 pixel index (after allowing for multi-pixel dithers to nearest integer) are summed over. The value of σ is adjustable; small values result in the best resolution possible, large values in compromised

resolution but lower background noise fluctuations. We selected $\sigma = 0.3$ by running a number of trials to optimize S/N for faint point sources taking into account the actual resulting PSF widths and background noise levels in combined images.

For each combined image an error array is carried that reflects the amount and quality of data going into any grid point accumulation:

$$Err_{xy} = \left[\sum_{i=1}^I \sum_{j=1}^J \sum_{n=1}^N gw_{i,j,n}pw_{i,j,n} \right]^{-1/2} \quad (4)$$

Our resulting PSF widths and background noise levels for the original epoch data are very similar to, but if anything marginally better (clearly better for the PC and F300W where our improved treatment of darks was probably significant) than the Version 2 drizzle release (Williams *et al.* 1996). Table 2 provides a quantitative comparison of results. Properties of the second epoch combined image were as expected: resolution the same as for the original epoch, and higher noise resulting from a factor of two less integration time in F814W.

EDITOR: PLACE TABLE 2 HERE.

Only for the PC1 F300W image combination are differences discernible between the two reductions of the first epoch HDF data from a careful visual inspection.

Image combinations for the second epoch were carefully compared with the first epoch equivalents for PSF widths, registration and noise level. No remaining systematic effects were found (except for the expected higher noise level in the second epoch). For some individual stars there are noticeable PSF differences between epochs, probably following from the rather meager sub-pixel x, y phase coverage provided by limited dithering for the first epoch HDF data. These differences are, however, small and not likely to cause

problems for SN searches in differences of first and second epoch combined images (and the minor differences are accounted for in control experiments discussed in §4.3).

3.6. Point Source Photometry

The final product of image combinations described in §3.5 are images still geometrically distorted as in the original data, but now $\times 4$ over-sampled, and scaled to the number of e-/pixel detected in a 6000 s exposure. The photometric transforms and basic integrity of these combined images were determined by: (1) The intermediate data products consisting of individual images scaled to e-/2700 s with corrections made for sky, scattered light, cosmic rays, and delta-darks were transformed back to DN/s using the same gain assumed in initial transforms to e-. This provides data frames that can be analyzed using standard prescriptions for WFPC2 photometry (e.g., WFPC2 Photometry Cookbook and WFPC2 DATA Analysis – A Tutorial, both available under the ST ScI Instruments WWW pages). (2) We selected the 11 Flynn *et al.* (1996) stars on WF2, WF3 and WF4 with magnitudes between $m_I = 19.0 - 25.5$; these stars never saturate in the F814W images and have adequate per exposure signal on the fainter stars. (3) Using *all* of the photometric corrections described in WFPC2 photometry documentation from ST ScI (0'.5 radius apertures, geometric distortion correction, CTE including time dependence, minor chip-to-chip normalizations, and transform to standard Johnson-Cousins *I* for F814W) magnitudes were computed for these 11 bright stars. (4) The same 11 stars are used to establish a photometric transform by adopting the magnitudes resulting from step (3) and measuring intensities in the over-sampled images using the same DAOPHOT parameters used in the SN searches to be detailed in §4.2.

Results from these photometric tests may be summarized as: (1) From the original epoch data our m_I magnitudes have a zero point shift of only 0.023 (sign of ours - Flynn)

and an rms scatter of 0.05 magnitudes relative to Flynn *et al.* (1996). (2) Across the two epochs our measures show a zero point offset and scatter of 0.015 magnitude. (3) Within cameras, transforming the over-sampled image photometry using DAOPHOT PSF fitting with a simple zero point offset relative to the known single-frame, aperture photometry derived values yields a scatter of $\sim 4\%$. We expect photometry errors on our SN detections to be dominated by random rather than any residual systematic errors.

For ease in comparing these results to other publications we note that the following transforms from our standard Johnson/Bessel-Cousins photometry apply:

$$m_{I,Vega-mag} = m_I - 0.035 \quad (5)$$

$$m_{I,AB(8000)} = m_I + 0.396 \quad (6)$$

$$m_{I,ST(8000)} = m_I + 1.220 \quad (7)$$

4. Supernovae Detection and Significance

The previous section outlined the steps taken to produce a single combined F814W image for each of the WFPC2 CCDs in both the original and second epoch HDF observations. The two epoch images (3200×3200 arrays for each CCD) are co-aligned to a small fraction of a pixel using extra-galactic sources and are normalized in intensity. A simple difference image therefore yields excellent cancellation for stationary, non-variable objects; those with changed position or brightness show intensity gradients or localized net intensity changes respectively. In this paper we are interested in detecting SNe and therefore search for point sources present in one epoch, but not the other. In addition the image combination process provided an error array; the image ratio of difference to error arrays provides a simple means of assessing the significance of intensity changes across

epochs.

4.1. Inspection of Difference Images

Both of the SNe detected in the HDF were first found via a rather casual inspection of direct, and in ratio to the error array, difference images. These two events remained the only convincing candidates following detailed systematic inspection of the difference images by both RLG and MMP. Figure 1 shows a small region around SN 1997ff in the first and second epoch direct images and the difference: second minus first. Figure 2 shows the same (both events were by chance in the second epoch) for SN 1997fg. A slightly broader perspective is shown for both events in Figure 3 which provides some qualitative indication (the two panels combined cover $\sim 2.4\%$ of the area surveyed on the WF CCDs) of the general quality of galaxy subtractions in these data. The stable PSF provided by *HST*, even across a time span of two years supports excellent cancellation of non-variable objects.

EDITOR: PLACE FIGURE 1 HERE.

EDITOR: PLACE FIGURE 2 HERE.

EDITOR: PLACE FIGURE 3 HERE.

Before providing quantitative details on SN 1997ff and SN 1997fg (previously announced in Gilliland & Phillips (1998)) we will now consider in turn a quantitative search for SN candidates in both epochs, null experiments designed to indicate at what level false signals may arise, and a quantification via artificial star additions to the real data of completeness as a function of object brightness and host galaxy redshift.

4.2. Quantitative Search for SN Candidates

We have used the DAOFIND, PHOT and NSTAR routines in DAOPHOT (Stetson (1987)) with parameters set appropriate to the PSF scale (FWHM of PSF = 5.7 pixels in our $\times 4$ over-sampled data) and general background noise level (~ 10 e- rms pixel-to-pixel for an over-sampled difference image scaled to 6000 s exposure time). A threshold of 6σ is used in DAOFIND which results in detection of “sources” well beyond the level at which real events can be reliably found. The candidate SN lists are then reduced using cuts in magnitude, magnitude error and the DAOPHOT sharpness statistic. The appropriate cuts were selected to maximize completeness in recovering artificially added stars, while at the same time allowing no sources to be claimed in control experiments designed to mimic potential noise sources, but for which no variation of sources across epochs was included.

A separate PSF was developed for each of the WF CCD cameras using 2-3 isolated, bright, but never saturated stars. Although WFPC2 shows small PSF spatial variance, we did not attempt to account for this; at the relatively low signal to noise of candidate SN the assumption of a spatially invariant PSF is warranted. Both the first minus second and opposite difference images are independently searched since DAOPHOT is structured to only find positive stars.

A primary cut in candidate SNe will be made using the magnitude error provided by NSTAR in DAOPHOT. There are two factors in addition to the mean background fluctuation level that need to be considered: (1) local errors will be larger in the difference image if an underlying object provided extra Poisson noise, or if an imperfect registration led to imperfect cancellation, and (2) the pixel-to-pixel errors are highly correlated in an over-sampled image.

It is instructive to consider at what level an increase of effective noise in the difference image arises from underlying sources. The sky rate in F814W averages 0.0446 e-/s per WF

pixel, over the sum of both epochs this yields an average of 8320 e-/pixel to which must be added equivalent readout noise of some 2820 e-/pixel from the 94 separate exposures. Therefore an underlying object will raise the errors by $2^{1/2}$ at a count rate per pixel of ~ 0.06 e-/s, which for the central pixel of a point source occurs at $m_I \sim 25.5$ (since our suspected SNe are well under this they do not significantly perturb the per pixel errors). This same count rate corresponds to an object with a surface brightness of $m_I \sim 21.8$ magnitude per square arcsec, which for a galaxy with half-light radius of $0''.3$ corresponds to a fairly bright (by HDF standards) 24th magnitude galaxy. Most of the surface area in the HDF is sky + readout noise dominated. Nonetheless, on bright galaxies there is added noise and we account for this by scaling the DAOPHOT reported magnitude errors with the PSF-weighted local value of the error array in ratio to the sky dominated value.

We account for the pixel-to-pixel noise correlation by renormalizing the DAOPHOT provided magnitude errors to average in the mean the standard deviation in magnitude of a large sample of added bright artificial stars (the required multiplicative factor is 2.0 for these $\times 4$ over-sampled data). The difference images show very little variation in mean, residual background level; we found that significantly smaller scatter in derived magnitudes of artificial stars resulted from forcing DAOPHOT to assume a constant (zero) sky level. Since the combined images have also been cleaned of cosmic rays, parameters in DAOPHOT were adjusted to not allow a dynamic re-adjustment of pixel weights normally used to reject cosmic rays during PSF fits.

4.3. Null Experiments (Controls)

Since we expected only order one to a few events in this project it is essential that a means be developed of quantifying the detection limit beyond which false events would begin to enter. We have designed two sets of control experiments with noise characteristics

very similar to the real two-epoch image differences, but for which no true sources can exist.

For the first of these null experiments we produced combined frames using the data from both epochs, but including in one set only the even numbered frames and in the other set the odd numbered frames. Difference images were then formed as usual between these two “epochs”. Any event with a timescale long compared to single exposures of ~ 2700 s should thus be canceled out. This uses the real data so noise characteristics must be the same overall, except in the real two epoch difference the exposure times are not balanced, and also any residual large-scale, systematic registration errors would enter differently than for the even-odd case. Another caveat arises if the exposure times in either epoch varied in an even-odd sense; in fact in the second epoch 1600 and 1900 second exposures were alternated so real epoch differences would survive, but at a reduced level of $\sim (300/1750)/3$ (at this level neither of the real SNe are detectable in the even-odd difference image). As with the real data, both the even-odd and odd-even difference images are analyzed with the DAOPHOT codes using the same control parameters as for the real data. Since such a test includes most, but not necessarily all sources of noise which could affect the real epoch differences, it is a necessary, but not sufficient condition to believe the claimed SN detections that no events be detected that are as significant in terms of the selection criteria of magnitude, magnitude error, and the sharpness parameter. With more relaxed selection criteria than will be used for final SN claims the most significant false signal from this even-odd control had $m_I = 27.86$, mag-err = 0.20, and sharpness = -0.19 – the magnitude is significantly fainter and the associated error larger than those for the two SNe found by inspection (and of course the quantitative DAOPHOT analyses).

Furthermore, this event was found near a CCD edge ($>90\%$ out from the center in y) and superimposed on a bright ($m_I = 21.4$), $z = 0.562$ galaxy. A minor defect exists in the scattered light subtraction that produces a small amount of extra noise (frame-to-frame so

it would be present in this even-odd control) at the location of bright objects at a CCD edge (one aspect in which our reductions are marginally poorer than the Version 2 drizzled images discussed earlier). We have now allowed for this (or other unrecognized systematics contributing to noise in the control experiments) by further biasing up the magnitude error by the ratio (if larger) of local noise in the control cases to the equivalent in the error array. This is a generally small effect, but properly accounts for lower confidence in regions with imperfect systematic reductions. This adjustment in magnitude errors appears throughout this paper.

The second type of control experiment is a direct attempt to simulate the data noise characteristics. The image model (using that from the first epoch only since we want the two simulated epochs to be identical except for independently added noise) is adopted as a noise-free representation of the image (true in comparison to single exposures), these are then used to generate a simulated data frame with Poisson and readout noise added on at each individual offset image position. These single images are then reanalyzed as with the real data frames (except the delta-dark was not added in and thus subtracted out) to produce combined first and second epoch images, the resulting noise characteristics do accurately reproduce the real difference images. Again it is a necessary, but not sufficient condition to believe the reality of the claimed SNe that this control experiment not show any events as significant. In this case the most significant event had $m_I = 27.85$, mag-err = 0.37 and sharpness = -0.07; again the magnitude is significantly fainter than for the claimed SNe and the mag-err much larger. This event happens to fall on an $m_I = 20.9$, $z = 0.764$ galaxy, not particularly close to the field edge.

The top 5 (in magnitude order) false alarm events (all detections from the control experiments with $m_I < 27.9$ and magnitude error < 0.4) are shown in Table 3. We must select criteria that will exclude all of the false signals found in the forward and backward

differences for both the even-odd and simulated data control experiments, but will first examine the more significant events found in the real data differences.

EDITOR: PLACE TABLE 3 HERE.

Table 4 shows the brightest 7 potential SNe detected in both epochs (all detections from the real data with $m_I < 27.7$ and magnitude error < 0.3). The candidate SNe in lines 3, 5, 6 and 7 of Table 4 are each clearly associated with diffraction spikes (at $\sim 1''$ distance) on the two brightest HDF stars that did not cancel out perfectly between the two epochs. No masking was applied near the bright stars in the DAOPHOT based search; the stable images provided by *HST* led to clean epoch-to-epoch differences with few spurious events that cannot simply be attributed to random noise. The two claimed SNe and the potential event on WF3 from line 4 of this table will be discussed in detail below.

EDITOR: PLACE TABLE 4 HERE.

4.4. Artificial Star Experiments (Completeness)

In order to assess our sensitivity to SN detection we have generated a large number of artificial star experiments adding in “SNe” of known brightness to the difference images (and with both signs as appropriate for first and second epoch events).

To avoid counting potentially spurious events that might arise from noise, thresholds have been set as $m_I < 27.7$, $\text{mag-err} < 0.2$, and $|\text{sharpness} \times \text{mag-err}| < 0.06$. These cuts eliminate (with considerable margin) all of the control experiment events listed in Table 3 as well as the only viable SN candidate (in addition to the two firm detections) listed in Table 4. In practice the simple limit on apparent magnitude is the most significant factor in

defining the final sample. We have tested for completeness for events that might come from very faint galaxies not visible even in the HDF by adding artificial stars at random positions over the field. In order to account for changes to noise characteristics due to galaxies (either through added Poisson noise, or through imperfect registration and subtraction) we have added artificial stars to galaxies identified in the Fernández-Soto, Lanzetta, & Yahil (1998) table and tracked completeness independently for the galaxy redshift ranges $0.0 < z < 0.4$, $0.5 < z < 0.9$, $1.0 < z < 1.4$, and $1.5 < z < 1.9$. Typical galaxy magnitudes are: $z = 0.2$, $m_I \sim 21$; $z = 0.7$, $m_I \sim 25$; $z = 1.2$, $m_I \sim 26$, and $z = 1.7$, $m_I \sim 27$ with the FWHM of magnitude histograms being about 3 magnitudes around the above medians. Galactic first moment radii have been adopted from Williams *et al.* (1996). We note that for a deVaucoulers' $r^{1/4}$ law for galaxy brightness distribution the half-light radius is one-half the first moment radius. The artificial SNe are added to the difference images with a random Gaussian position distribution such that each has a 50% chance of falling inside the half-light radius. We have also preferentially added the artificial SNe with a frequency proportional to the galaxies' intrinsic brightness within each redshift bin. The number of added SNe (both epochs) totaled 64, 322, 262 and 230 for the $z \sim 0.2$, 0.7, 1.2 and 1.7 redshift bins respectively. The random positions were set once for each galaxy redshift range and then held fixed for independent additions at the different magnitude levels.

Table 5 shows the completeness limits derived from these artificial SN experiments. The results for both epochs have been averaged with no difference having been noted between the two epochs. The completeness level for artificial SNe added into blank regions of the HDF is well represented by the limits for the $z = 1.7$ galaxy-redshift bin; at this galaxy brightness the difference image noise level is set by sky plus readout noise and is little influenced by an underlying faint galaxy. While $m_I \sim 27.5$ (at high z) is about the 50% completeness level *for which we are also confident that objects brighter than this have little chance of having arisen from noise*, the actual detection levels with DAOFIND are

about one-half magnitude deeper. For example at $m_I = 27.9$ the DAOFIND search phase returns 30% and 40% of the added artificial SNe at $z = 0.7$ and 1.7 respectively, but since our magnitude cut is well above this only the few having extracted magnitudes too bright by >0.2 magnitude and with errors < 0.2 magnitudes are counted in Table 5.

EDITOR: PLACE TABLE 5 HERE.

4.5. SN 1997ff, SN 1997fg

We have shown the direct and difference images for SN 1997ff and SN 1997fg in Figures 1 – 3 and in previous sections presented arguments related to significance of the detections. In this section we further develop the case for the events being SNe in host galaxies at high redshift.

A SN candidate should pass several tests: (1) Signal level well above background fluctuations and above the level at which false alarms in similar searches would begin to show up. (2) The point spread function should have a distribution similar to that of other stellar sources in the field. (3) The objects should be detectable in independent subsets of the data including divisions in which different dither positions on the CCD were used. (4) The object intensity should show changes (or near constancy) over the multi-day observing interval consistent with expectations for a SN light curve transformed to the appropriate redshift (intensity adjusted including appropriate K corrections, and dilated in time). (5) If located in an obvious galaxy the SN candidate should be positioned such that active galactic nuclei (AGN) fluctuations are not an equally, or more likely explanation of the intensity change.

We have argued above that the two SN candidates satisfy the first test – the

quantitative magnitudes and associated errors returned with DAOPHOT processing are significant when compared to our sensitivity to spurious events arising from noise. A simpler approach of placing small apertures on the SN candidates and ratioing the aperture counts to the error from enclosed background fluctuations shows significance near 20 and 9 σ for SN 1997fg and SN 1997ff respectively.

Figure 4 shows radial profiles for the two SN candidates from difference images and similar profiles for nearby stars from the second epoch direct images. For each of the SN the profiles are stellar in appearance and Gaussian fit widths for the SNe are the same to within expected errors (i.e., fit would not be significantly worse if the width were forced to the stellar value) as for bright stars. (Note also that a Gaussian fit is a rather poor approximation in detail to the stellar profiles underestimating both the inner core and the wings.)

EDITOR: PLACE FIGURE 4 HERE.

The second epoch observations were taken in three separate *HST* visits each of six orbits with a total separation of three days. The two claimed SNe are apparent from inspection of each of these three separate averages, each of which had an independent set of dithers. The claimed SNe events clearly do not arise from isolated noise events. The individual daily magnitudes are given in Table 6 for the two SN.

We adopted a different strategy than DAOPHOT analysis of the over-sampled, combined data for analysis of the time-resolved magnitudes. Photometric precision, or integrity of the combined images relies on having a dense sub-pixel dither distribution on the spatial scale of the weight kernel of Eq. 3 – this is well satisfied for the full epoch stacks, but starts to break down for the daily averages. To account for this we adopted the approach of using DAOPHOT to generate an over-sampled PSF at the position of the

SN as determined from the full epoch fit. We then used the individual time-series data frames (with cosmic rays eliminated and all other corrections made) in conjunction with known dithers for each frame to place each pixel center in a 4×4 pixel region near each SN relative to the PSF from which an appropriate estimate of the PSF was interpolated. In this approach a full least-squares point spread function fit was determined as a direct summation over individual pixels in the stack. Since this allowed full use of positional information, precision of the final results was not dependent upon having a dense sub-pixel distribution of under-lying dithers. A separate zero point calibration for each day and CCD was determined by analyzing the known bright stars. Analysis of the difference image data as required for the SNe additionally required subtracting a first epoch intensity value determined for each x, y position from interpolation in the over-sampled, complimentary epoch image. The mean magnitudes given in Table 6 follow from the same procedure, but over the full data stack, and are thus independent from the Table 4 results from DAOPHOT. Using DAOPHOT on single-day, combined images gave similar, but somewhat noisier results.

EDITOR: PLACE TABLE 6 HERE.

Figure 5 shows the daily photometry values overplotted on canonical SNe Ia light curves adjusted in magnitude and time dilated according to the host galaxy redshifts and assumed cosmology ($\Omega_M = 0.28$, $\Omega_\Lambda = 0.72$, $h = 0.633$, $M_B = -19.46$) and intrinsic SN Ia peak brightness. The date of peak brightness has been arbitrarily shifted to have the observed values fall on the light curve on the descending branch. The magnitudes for both SNe show a decline (only marginally significant) easily consistent with the ~ 0.1 magnitude decline expected during this time on the declining branch. At the same magnitude relative to peak brightness on the rise an ~ 0.4 magnitude brightening would be expected over the three day interval which is inconsistent with the data. The observed time-resolved

magnitudes are entirely consistent with interpretation as SN Ia slightly past peak intensity.

EDITOR: PLACE FIGURE 5 HERE.

We have adopted the Fernández-Soto, Lanzetta, & Yahil (1998) redshift for 4-403.0 based on their use of 7 color ($UBVIJHK$) photometry to develop photometry-redshift relations; Connolly et al. (1997) have also emphasized the need for near-IR colors in determining photometric redshifts over $1 < z < 2$. For 4-403.0 the IR (JHK) intensities from the work of Dickenson et al. (1999, in preparation) are 2.5 – 3.5 magnitudes brighter than in the optical. Sawicki, Lin, & Yee (1997) based on a photometric redshift technique using only the direct HDF $UBVI$ photometry determined a redshift of $z = 0.95$ (their object 40368). Our interpretations will assume the $z = 1.32$ value for SN 1997ff, although we note that without a spectroscopic determination this must be viewed with caution. The Fernández-Soto, Lanzetta, & Yahil (1998) photometric redshifts show an *rms* dispersion of $\sigma = 0.09$ in comparison with a sample of ~ 100 spectroscopic redshifts at $z < 2$, and no cases were discordant at $> 3\sigma$.

SN 1997ff is located $0''.11$ west and $0''.11$ south of the center of galaxy 4-403.0 (Williams et al., 1996). This galaxy is very red at $v - i = 1.64$ and is classified as an elliptical galaxy on the basis of colors and template fitting by Fernández-Soto, Lanzetta, & Yahil (1998) (no. 690 in their table) with a photometrically determined redshift of 1.32. Close inspection of this image in a multi-color representation of the HDF shows nothing to suggest anything other than a normal, isolated elliptical galaxy. Williams et al. (1996) give a first moment radius of $0''.25$ for 4-403.0 which translates to a half-light radius of $0''.125$ assuming an $r^{1/4}$ law, thus the SN falls near the half-light radius. Given the galaxy characteristics, and the clear off-center location for the brightening, interpretation as a SN is much preferred over an AGN brightening. As shown in Figure 5 the observed brightness for SN 1997ff is about

two magnitudes below the peak luminosity expected for a SN Ia.

SN 1997fg is located $0''.31$ east and $0''.31$ south of the center of galaxy 3-221.0. This galaxy was assigned a neutral color of $v - i = 0.74$ and is classified as an irregular by Fernández-Soto, Lanzetta, & Yahil (1998) (no. 599) with a spectroscopically determined redshift of 0.952 (Cohen et al. (1996)). In this case the galaxy morphology is not simple. The claimed SN event is well offset from primary light concentrations, the SN produced a factor of two local brightness increase relative to the underlying galactic light at the $0''.1$ spatial scale. There is no reason to suspect an AGN interpretation for this event. At nearly 2.5 magnitudes below the peak brightness expected for a SN Ia at $z = 0.95$ this event could arise from other types of SNe, in particular the galaxy type and event brightness would be consistent with a SN II event. We will provide further arguments in §5 to quantify the relative probability that this was a SN Ia or SN II event.

4.6. Other SN Candidates in the HDF

To the level of our conservative magnitude and error cuts used to quantify completeness limits ($m_I < 27.7$, error < 0.2 magnitudes) there are no additional candidates once obvious artifacts from diffraction spikes on bright stars are excluded. The event for the 4th line of Table 4, however, deserves further investigation as the next most likely SN candidate. The event with $m_I = 27.35$ and an associated magnitude error of 0.284 is apparent as a brightening near the core of a $z = 0.52$, $m_I = 23.60$ galaxy number 3-404.2 with a half-light radius of $0''.15$. Table 5 shows that at this magnitude and redshift artificial SNe are only recovered at an efficiency of $\sim 25\%$. False alarms from our control experiments fall short by 0.5 magnitudes in reaching this level however, thus putting this event in a grey area relative to our reasonable, but somewhat arbitrary choice of selection criteria.

The position of the 3-404.2 excess light in the first epoch is only $0''.048$ from the galaxy center, since this galaxy has an elongated shape and the candidate SN signal is weak the measured offset from the nucleus is not considered significantly different from zero. The amount of light interior to a radius of $0''.05$ for galaxy 3-404.2 is $\sim 4\%$ of the total. These facts suggest an alternative interpretation as an AGN is preferred. We have performed an analysis comparing the change in total intensity within the half-light radius of 3-404.2 across epochs (4.9%) with expected noise levels (1.2%) at this galaxy brightness from simulations, thus establishing at $\gtrsim 4 \sigma$ that this galaxy did exhibit a real intensity variation – most likely from nuclear activity, although we cannot rule out a SN interpretation.

An additional variable source, galaxy 2-251.0, is evident from a casual inspection of the two epoch F814W difference image. This bright ($m_{AB(814)} = 21.3$), compact source only marginally resolved at WFPC2 resolution has been widely discussed in the literature as an AGN. The optical spectrum yields a redshift of 0.960 (Phillips et al. (1997)) and shows broad Mg II emission and other weaker features consistent with nuclear activity. In the radio it displays a core size $< 0''.1$ and is variable by about 30% over 18 months (Fomalont et al. (1997), Richards et al. (1998)), and it is a strong IR source detected by ISO (Rowan-Robinson et al. (1997)). Using an aperture of $0''.5$ we find that 2-251.0 shows an optical increase of 8% from the first to second epoch and that in comparison to the expected measurement noise this is significant at $\sim 7 \sigma$. The brightening comes from an unresolved source that is coincident with the galaxy core. If this probable AGN variation were attributed to a SN event instead, it would have $m_I \sim 23.5$, or just marginally brighter than a Type Ia peaks at for this redshift. The object is detected in our DAOPHOT search, but after error scaling as discussed in §4.3 has a magnitude error in excess of unity and is not retained. The two-epoch difference image of 2-251.0 is sharp, but not well matched by a PSF – a detailed examination shows that the sub-pixel sampling of the first epoch data was unusually poor at the position of 2-251.0 yielding low confidence in details of the resulting

difference image morphology. In this case we cannot rule out a SN event at $m_I \gtrsim 23.5$ near the core of 2-251.0, but given the abundant evidence consistent with an AGN interpretation have no reason to expect such. This example of potential incompleteness in our SNe search is directly accounted for in the completeness limits as tabulated in Table 5.

We do not see credible evidence for additional SN events in the two HDF epochs. The stable *HST* point spread function over time and the uniquely well-dithered and deep data in both F814W epochs on the HDF have supported accurate quantification of completeness limits.

5. Modeling the Expected SNe Rates

In the previous section we quantified the brightness levels at which point sources present in only one of the two HDF epochs could be detected. The number of expected SNe in the HDF at a given epoch depends upon: (1) the SN rate per unit redshift and (2) modeling of the length of time SNe at different redshifts will remain above the established detection threshold. Several recent theoretical studies have addressed the expected variation of both Type Ia and II rates as a function of redshift. Typical of these is the work of Madau, Valle, & Panagia (1998), who model the SN rate by using observed luminosity densities in the universe to imply a star formation history. With an assumed initial mass function this in turn implies the number of stars more massive than $8 M_{\odot}$ which on short time scales become Type II SNe. Type Ia events are modeled as following from binary evolution in which double white dwarfs merge, or single degenerates evolve over the Chandrasekhar mass through accretion of mass transferred from their companion. With parameterized delay times in the range 0.3–3 Gyr for this evolution after White Dwarf formation from 3–8 M_{\odot} stars (see also Ruiz-Lapuente & Canal (1998), Sadat et al. (1998), Yungelson & Livio (1998), Dahlen & Fransson (1998)) this fixes the rate of Type Ia events.

Modeling the length of time SNe at different redshifts will remain above our detection threshold in the HDF requires knowledge of both the light curves and spectral evolution. Our observational understanding of SNe Ia has grown during the last 10 years to the point where it is now possible to carry out relatively precise predictions of the visibility of these events as a function of redshift. Calculating such “detection windows” for SNe II is, unfortunately, more difficult due to their extremely heterogeneous nature. To date, only a few attempts have been made at carrying out such calculations for either type, and these have generally assumed black-body (or cutoff black-body) spectra for the SNe (e.g., Miralda-Escudé & Rees (1997); Dahlen & Fransson (1998)). In this section we must, therefore, develop the machinery necessary to translate observational knowledge of typical SN light curves and spectra into realistic detection windows. For these simulations we have ignored Type Ib/Ic SNe, but note that future studies with higher detection statistics should include these types as well.

5.1. Type Ia Supernovae

The magnitude of a SN Ia in filter X can be expressed as follows:

$$m_X = M_B(t, s) + K_{BX}(z, t, s, A_B) + \mu(z, \Omega_M, \Omega_\Lambda, H_o) + A_B. \quad (8)$$

Here t refers to the epoch when the SN Ia is being observed, s is the stretch-factor (as described in Perlmutter et al. (1997)), z is the redshift and A_B is the reddening in the host galaxy. The extinction in our galaxy in the direction of the HDF is negligible and thus is not included. The stretch-factor, s , has three effects on the supernova. First, it is responsible for changing the shape of the light-curve. From an $s = 1$ template, which is similar to the Leibundgut template for SNe Ia (Leibundgut, 1988), all known light-curves for SNe Ia can be reproduced quite reasonably from the U -band through the V -band (over the time range of -18 days to +40 days with respect to maximum light) by stretching the

time axis of the light-curve about maximum light by the factor s . Second, a relationship exists between the peak magnitude in B for a SN Ia and s that can be expressed as follows:

$$M_B = M_B(s = 1) - \alpha * (s - 1). \quad (9)$$

This is the same relationship found by Phillips (1993) and studied by Riess, Press, & Kirshner (1995) where a correlation between the peak brightness and the decline of the light curve from maximum light to +15 days ($\Delta m_{15}(B)$) was presented. The broader light curves (smaller $\Delta m_{15}(B)$) are intrinsically brighter, and the narrower light curves (larger $\Delta m_{15}(B)$) are intrinsically fainter. From Perlmutter et al. (1997), the relationship between $\Delta m_{15}(B)$ and s is:

$$\Delta m_{15}(B) = 1.96 \pm 0.17(s^{-1} - 1) + 1.07 \quad (10)$$

We adopt $M_B(s = 1) = -19.46$ from Sandage et al. (1996), Hamuy et al. (1996a), and Suntzeff et al. (1999, in press), and $\alpha = 1.74$ from Perlmutter et al. (1999). Finally, there is a relationship between the color of SNe Ia and s which can be expressed as follows:

$$B - V = -0.19 * (s - 1) - 0.05. \quad (11)$$

This equation shows that the broader, brighter SNe are slightly bluer as well (see also Phillips et al. (1999)).

The biggest challenge in determining the observed magnitude is in performing an accurate K-correction. For this search, using the F814W filter and going to magnitudes fainter than $I = 27$, it is necessary to calculate K-corrections out to $z = 2.0$. This means knowing the flux as a function of time for a SN Ia down to $\approx 2000 \text{ \AA}$. As can be seen from Eq. 8 the K-correction is dependent not only on z and t but on s and A_B as well. The affect of the former two variables are obvious: differing redshifts and spectra (due to temporal evolution) will change the resultant K-correction. The latter two are secondary effects which can be thought of as ‘‘color terms’’ (the weighting of the combined spectrum and system

throughput changes for spectra with different colors brought about by extinction and/or stretch variations). In Figure 6 we show the light-curves of extinction-free, $s = 1.0$ SNe Ia between $0.25 < z < 1.75$ along with a line which demarks a limiting detection magnitude of $I = 27.3$. Note how SNe Ia with $z < 0.50$ are visible for over a year given this limiting magnitude.

EDITOR: PLACE FIGURE 6 HERE.

These light curves were produced by gathering together all the spectra of well observed SNe Ia currently available to the authors. Especially important to these calculations were the SNe observed in the UV by IUE and HST (Cappellaro, Turatto, & Fernley, 1995; Kirshner et al., 1993). A set of standard photometric templates were then created for a $s = 1.0$ SN Ia in $UBVRI$. The spectra were then “flux calibrated” in order to reproduce the observed magnitudes of these template light curves by both adjusting the zero point of the flux scale and applying a slope correction to the flux so that each spectrum would have the correct color (Riess, Press, & Kirshner (1996)) for a particular phase. The slope correction was performed by altering the flux using the reddening law of Cardelli, Clayton, & Mathis (1989) (either making them bluer or redder accordingly). Interpolation between these spectra from 14 days before to 45 days after maximum light was performed from 2000 to 10000 Å. Outside of this range a simple extrapolation of the data was used to complete the light curves.

To calculate the K-correction for a different stretch value at time t two steps are involved. First, instead of using the spectrum at time t , one uses the spectrum from the “stretched time”, t_s where $t_s = s \times t$. Second, one “color corrects” the spectrum from t_s according to Eq. 11. The resultant spectrum is the one used to perform the K-correction. Ideally, in order to calculate K-corrections as a function of the stretch factor, we would

like a library of spectra covering all wavelengths and epochs of interest and have it be representative of the full range of observable decline rates. This is not possible with the data available to us today. However, as will be shown in Nugent et al. (1999, in preparation), the color of the spectrum is the most important factor in getting the K-correction right for a SNe Ia. By using this fact it allows us to combine different stretch spectra into one template and get the wavelength and phase coverage which we need to perform these calculations. By following these procedures it is possible to produce K-corrections to the B and V bands from R and I band data to a $z \approx 1.0$ which are good to 0.01 mag. The R and I light curves were stretched in a similar fashion as the UBV light curves. While this is a rather crude approximation for these two bands (good to 0.2 magnitudes on any given day over the first 60 days of the light curve for a given stretch supernova) it does not affect the results of this work strongly. This is due to the fact that past a redshift of 0.3 the K-corrections to the F814W filter are done using rest-frame spectroscopy bluer than what occurs in the restframe R-band. At higher redshifts, when one becomes more strongly dependent on knowledge of the UV, the accuracy of this technique is strongly influenced by the quality of data (in particular the flux calibration) obtained by the IUE.

Given the ability to calculate a light-curve over the necessary redshift range, we now turn our attention to the expected rate of SNe Ia. The observed rates for SNe Ia have been studied by Cappellaro et al. (1997) for $z \lesssim 0.1$ and at higher redshift, $z \approx 0.5$, by Pain et al. (1996, 1999, in preparation). We will use the rates from the latter work as they are the most accurate available to date, and are based on the CCD searches by the Supernova Cosmology Project (SCP) which are similar in nature to the type of search performed in the HDF. The evolution of this rate as a function of redshift (especially for $z \gtrsim 1.0$), is sensitive to both the SFR and details of the progenitor model. We will ignore this effect for now and make the assumption that the rate of SNe Ia per unit volume is constant as a function of redshift and can be expressed as 2.39×10^{-5} SNe Ia/year/Mpc³ at $z=0.5$ (restframe). We

will assume the following cosmology: $\Omega_M = 0.28$, $\Omega_\Lambda = 0.72$, and $h = 0.633$ as our standard.

We do not expect the volume rate of SNe Ia to be constant between $0.0 < z < 1.5$, none of the models predict this. However, by assuming a constant rate per volume which is normalized at $z = 0.5$, we may be either underestimating or overestimating the rate at $z = 0.95$ or $z = 1.32$ (see Fig. 1 in Dahlen & Fransson (1998) or Fig. 3 in Sadat et al. (1998)) and at some level assuming a constant rate can be viewed as the conservative approach. Finally we note that in contrast with most theoretical studies postulating an increasing rate of both Type Ia and II rates to $z \sim 1 - 1.5$ with only a modest decline by $z \sim 2$, Kobayashi et al. (1998) argue for a strong metallicity dependence on the mechanism allowing white dwarfs to accrete material. This provides a cutoff to SNe Ia for $[\text{Fe}/\text{H}] \lesssim -1$ and predicts a steep dropoff in the cosmic SN Ia rate near $z \sim 1.3$.

In order to compare the rates observed with a theoretical rate the following three assumptions were made. (1) SNe Ia have an intrinsic stretch corrected dispersion of 0.15 magnitudes (Hamuy et al. (1996b), Riess, Press, & Kirshner (1995)). (2) The luminosity function can be approximated using a Gaussian distribution in stretch with a $\sigma = 0.05$ (Perlmutter et al. (1999)). (3) The reddening distribution is the same as seen in Hatano, Branch, & Deaton (1998). A Monte Carlo simulation of the HDF search was then performed using these parameters coupled with the rate of SNe Ia mentioned above and the detection efficiencies described in §4.4.

The results are displayed in Figure 7. Out to $z \sim 0.4$, essentially all but the fastest declining SNe Ia would be detectable in the HDF with HST for 1+ years. Hence, our search is complete at these redshifts, and our simulation predicts a rapid increase in the observed SN Ia rate out to this redshift due simply to the increasing volume that is being surveyed. At redshifts beyond $z \sim 0.4$, a typical SNe Ia ($s = 1$) becomes observable for a steadily decreasing fraction of a year, reaching 50% at $z \sim 1$ and 20% at $z \sim 1.5$. Hence,

incompleteness becomes more and more important. However, even ignoring incompleteness, the observed rate should begin to flatten out or turn down (depending on the exact cosmological parameters) due solely to geometry (dV/dz) and time dilation ($1/(1+z)$). These effects combine to give the flattening and strong turn down in Figure 7 which occurs between $0.5 < z < 1.7$. Beyond $z \sim 1.75$, the steep flux decline observed below 260 nm in the maximum-light spectra of SNe Ia, produces a final, rapid cutoff below detectability.

EDITOR: PLACE FIGURE 7 HERE.

The long time period for which SNe Ia at $z \lesssim 1.5$ are above our detection threshold (see Figure 6) has as a consequence that most discoveries are expected for events well past maximum brightness. The I-band magnitude at peak and magnitude at discovery are shown in Figure 8 for this simulation of the HDF search. Note that very few SNe are discovered before maximum due to the fact that this is the time when the light curves are evolving the fastest in brightness. Conversely, at epochs (and magnitudes) in the light curve where the brightness evolution is changing the slowest (i.e., around maximum light and during the final exponential decline phase), the “magnitude at discovery” points are observed to “pile up”.

EDITOR: PLACE FIGURE 8 HERE.

From Figure 7, we conclude that in a forward and backward search of the HDF, ~ 0.32 SNe Ia should have been discovered. Due to small number statistics, this result is completely consistent with the observations. Note that the expected detection frequency of SNe is a strong function of adopted cosmology as illustrated in Figure 9. The upper curve of Figure 9 reproduces the distribution shown in Figure 7 for our Ω_Λ dominated cosmology which yields expected rates of $\sim 50\%$ and $\sim 100\%$ higher than for open and flat $\Omega_\Lambda = 0.0$

universes respectively. The observed rate would therefore serve as a strong discriminator of cosmological world models if the true rate per unit volume were constant with lookback time as we have assumed. However, as mentioned, the SN Ia rate should reflect the evolution of the SFR in the universe with a time delay which is related to the progenitor lifetime. Depending on details of the exact redshift dependence of the SFR (see next section) and the typical lifetime, τ , of SN Ia progenitors (which currently is a free parameter in the range $0.3 \lesssim \tau \lesssim 3$ Gyr), increases of up to a factor of ~ 2 – 10 in the rest-frame SN Ia rate per unit volume are expected out to $z \sim 1$ and beyond (e.g., see Dahlen & Fransson (1998); Sadat et al. (1998)).

EDITOR: PLACE FIGURE 9 HERE.

5.2. Type II Supernovae

There are many advantages in calculating the rates of SNe Ia. The light curves and spectra are homogeneous and well observed from the UV through optical. They are among the brightest SNe having a narrow spread in luminosity and, in general, they lack strong extinction. Finally, the local rates are becoming fairly well established with the myriad of CCD SNe searches currently being conducted. All of these advantages vanish when one works with SNe II. They are a heterogeneous class of objects. The number of high-quality observations is small, especially in the UV. One should make note that while the Type II SN 1987A was by far the best observed supernova of any type, it would almost never be seen in even the deepest of supernovae searches, being ≈ 5 magnitudes fainter than the typical SN Ia. (In the HDF search an 87A event would barely be detectable at a $z = 0.5$). In addition, it is almost considered in a class of its own, thus practically useless in providing information necessary for K-corrections or light curve shapes. Lastly, the local

rates of SNe II are poorly established due to a complete lack of knowledge concerning the luminosity function of these objects. Even the very deep high-redshift SNe searches have not yet made significant inroads in understanding the rates of SNe II. An example of this can be seen in the work of the SCP, where over 80 SNe Ia have been discovered yet only 5 SNe II have been positively identified spectroscopically, and all with $z < 0.45$. Out of 95 probable SNe reported in a sample of IAU Circulars by the High-Z team 45 are confirmed SNe Ia with precise redshifts, while only 10 are confirmed SNe II and another 10 possible SNe II all with $z < 0.45$. Given all of these obstacles, the major focus of this section will be to highlight the techniques necessary to solve for the rates of SNe II at high-redshift. At present, any rate determination should be viewed skeptically, as it is strongly dependent on several assumptions whose basis is shaky at best.

The major problem we face concerning SNe II is their heterogeneity. In general SNe II can be broken down into two classes, plateaus (SNe II-P) and linears (SNe II-L) a classification which is based on the shape of their respective light curves. Within these sub-classifications Miller & Branch (1990) showed that the dispersion in peak brightness in the B -band is more than a magnitude. These dispersions are most likely not gaussian and are brought about by two different factors. First, SNe II are the result of a core collapse of a massive star. These stars can range in mass by an order of magnitude when they explode, resulting in very different light curves and peak magnitudes. Second, most SNe II suffer from host galaxy extinction due to the fact that they are massive stars located in regions of active or recent star formation. As Miller & Branch (1990) pointed out in their conclusions this fact further complicates matters since the true dispersions could be larger or smaller due to extinction — larger if the brighter SNe II in their sample preferentially suffered from extinction, and smaller if extinction only affected the fainter ones. Finally they noted that the true mean magnitudes would likely be fainter due to the loss of faint SNe from the observational sample.

Heterogeneity also plays a role in the K-corrections. While classical SNe II-P show generally similar spectral evolution, details such as the time spent on the plateau portion of the light curve can vary considerably from event to event (Patat et al. (1993, 1994)). Type II-L SNe display even less homogeneity, and narrow emission line SNe II (type IIIn), which we do not even consider here since they are relatively rare, and are even more diverse in their characteristics. Of the 49 SNe discovered in the Calan/Tololo survey only 4 were classified as Type IIIn (Hamuy (1999, private communication)). In addition, UV data for SNe II (with the exception of SN 1987A) is practically non-existent.

Given this diversity, we are forced to make a number of simplifying assumptions in our simulations. We start by considering a universe which produces Type II-P and II-L SNe only. For each event, we generate a rest frame absolute B magnitude using the mean magnitudes and dispersions of Miller & Branch (1990) which are uncorrected for reddening. Given our cosmology this translates into $M_B = -16.90$ with a $\sigma = 1.39$ for SNe II-P and $M_B = -17.42$ with a $\sigma = 1.32$ for SNe II-L. We assume that each SN is affected by the same amount of reddening, $A_V = 0.45$ mag, which is the average value found by Schmidt et al. (1994) in their study of 16 SNe II-P and II-L. We also adopt mean light curve shapes for these two classes using the templates given by Cappellaro et al. (1997). For the K-corrections, the best one can hope to do is provide a correction whose uncertainty is smaller than the dispersions mentioned above and represents in an average way the “typical” K-correction for a SNe II at a given epoch. To this end spectrum synthesis calculations using the non-LTE code PHOENIX 9.0 (Hauschildt et al., 1997; Hauschildt, Baron, & Allard, 1997) were carried out by PEN. The spectra of SNe 1979C (Cappellaro, Turatto, & Fernley, 1995), 1992H and 1993W (courtesy D. Leonard) were fit at several epochs. The resultant fits of these spectra provided a nice match to the observed data. The major emphasis of this effort was to model the UV as well as possible. The calculations modeled the atmospheres by assuming a 15 to 25 M_\odot progenitor, solar abundances and

exponential density profiles.

Many in the past have made the assumption that the spectra of SNe II can be modeled by a blackbody with a given effective temperature (T_{eff}). While this *might* be appropriate at very early times it definitely begins to fail after the first ≈ 2 weeks. For example, Miralda-Escudé & Rees (1997) modeled the spectrum of a SNe II-P during its plateau phase by a blackbody curve with $T_{eff} = 7000$. In Figure 10 we present a spectrum synthesis fit to SN 1993W at 40 days along with a $T_{eff} = 6000$ blackbody curve which best represents the spectrum in the optical region ($T_{eff} = 7000$ was too hot for this particular supernova). Overlaid is the effective coverage of the F814W filter for this supernova if it occurred at a $z = 1.0$. As one can plainly see the simple blackbody curve poorly represents the flux of the supernova in this region. In the UV the spectra of most supernovae are dominated by the effects of iron-peak ionic species. The UV opacity is a product of thousands of iron-peak spectral lines which significantly depress the flux with respect to the continuum. In Figure 11 we highlight this effect by presenting the *I*-band magnitudes as a function of redshift at day 40 (in the middle of the plateau phase) for both a $T_{eff} = 6000$ blackbody curve and our spectrum synthesis calculation. Both spectra are calibrated to have $M_B = -16.27$, an average magnitude at this phase given our cosmology. The first thing to note is the crossing point of these two lines. It occurs at a $z \approx 0.8$ and marks the location where the F814W filter best matches the rest-frame *B*-band filter. Below this redshift one is sampling the optical and IR portion of the spectrum. One can see that a blackbody curve does a reasonable job here with the difference in magnitudes never exceeding 0.35. Above this redshift one samples the redshifted UV. At a $z = 1.5$ there is already a 2.25 magnitude difference between the curves with the blackbody curve being significantly brighter. This shows the danger in using these simple approximations for any reasonable rate calculation which relies on knowledge of the UV.

EDITOR: PLACE FIGURE 10 HERE.

EDITOR: PLACE FIGURE 11 HERE.

Given the library of spectra generated from our spectrum synthesis calculations, we apply a reddening of $A_V = 0.45$ mag to each and then scale the spectra to match the M_B magnitudes generated from the Miller & Branch (1990) distributions and the Cappellaro et al. (1997) template light curves. In Figure 12 we present, for comparison purposes to Figure 6, the resulting average SN II-P and SN II-L light curves as a function of redshift. While on average the SNe II-L's are more than half a magnitude brighter at maximum light, the SNe II-P stay above a given magnitude for a longer time due to the plateau phase. In the HDF search, given the long baseline between reference and discovery images, they become much more likely to detect.

EDITOR: PLACE FIGURE 12 HERE.

Given a method for calculating light curves we now turn our attention to the rates of SNe II. Two questions must be addressed: (1) what is the local rate of SNe II, and (2) how much does the SFR change over the range in redshifts we are concerned with in the HDF search ($0.0 < z < 2.0$). The latter question is highly relevant since it is believed that the production of SNe II is strongly coupled with the SFR. The results of Cappellaro et al. (1997) show that the local rate of SNe II (with rather large uncertainties) is a factor of 2.5–3.0 greater than that of the rate for SNe Ia. For the latter, we again assume the Pain et al. (1996, 1999, in preparation) rate (bearing in mind that this value applies at $z \sim 0.5$, and therefore may be an overestimate of the local SN Ia rate), which implies that locally we have 6.5×10^{-5} SNe II/year/Mpc³. We will follow the work of Cappellaro et al. (1997)

and divide this number equally into SNe II-L and SNe II-P. We now must consider how the evolving SFR affects this number.

In Figure 3 of Madau, Pozzetti, & Dickinson (1998) we see the evolution of the luminosity density, ρ_ν , as a function of redshift for a flat cosmology with $\Omega_M = 1.0$ and $h = 0.50$. Over the range $0.0 < z < 2.0$ there is a factor of 10 increase in ρ_ν in the UV. This corresponds to a similar increase in the SFR. The lower redshift data ($z < 1.0$) comes from the work of Lilly et al. (1996) and suggests a rather steep evolution in the SFR to $z = 1.0$ and beyond when combined with the work of Connolly et al. (1997). In both Gronwall (1998) and in Treyer et al. (1998) evidence is presented that the local abundance of star forming galaxies has been underestimated and that the SFR only increases by a factor of 4 not 10 over this range. We adopt this newer, more conservative value for our calculations. This factor of 4 is further reduced to ≈ 2.3 when one moves into the Λ dominated cosmology we subscribe to in this paper (see Figure 13).

EDITOR: PLACE FIGURE 13 HERE.

Taking this into account we can modify the local rate mentioned above and arrive at an average rate at $z \sim 2$ of 1.5×10^{-4} SNe II/year/Mpc³. Combining this with the details of the light curve calculations we ran simulations for both SNe II-L and SNe II-P detections in the HDF. The results of these can be seen in Figures 14 and 15. We have placed the graphs on the same scale to illustrate how much easier it is to discover the SNe II-P in this type of search. The results of these simulations predict that, on average, 0.47 SNe II-L and 0.70 SNe II-P will be discovered in an HDF style search.

EDITOR: PLACE FIGURE 14 HERE.

EDITOR: PLACE FIGURE 15 HERE.

5.3. Implications for SNe 1997ff and 1997fg

Lacking either spectra, or significant photometric time-series information for SNe 1997ff and 1997fg interpretation as Type Ia or II depends upon environmental and statistical factors which we summarize here.

Figures 16 and 17 provide histograms of the relative number of SNe detected per magnitude interval in the HDF at host redshifts of $z = 0.95$ and 1.3 respectively following from simulations as described in §5.1 and 5.2. The statistical probability that any given event corresponds to a particular SN type is a strong function of both magnitude at discovery and redshift. For $z = 0.95$ (Fig. 16) it is interesting to note that for $m_I \sim 24$ most events are Type Ia – this is broadly consistent with results of ground-based searches which at this redshift and magnitude level are dominated by Type Ia events. At the fainter magnitudes to which our HDF search is sensitive the relative probability switches such that at $m_I = 26$ both Types II-L and II-P are statistically a factor of 2 more likely than a Type Ia. For $z = 1.3$ (Fig. 17) similar behavior holds, although shifted to fainter discovery levels in general and compressed in range due to our cutoff near $m_I \sim 27.5$.

EDITOR: PLACE FIGURE 16 HERE.

EDITOR: PLACE FIGURE 17 HERE.

The general prevalence of expected Type II events relative to Type Ia at high $z = 1.3$ and faint magnitudes is counter-intuitive given results from ground-based searches and the recognition that Type Ia events peak on average 2 magnitudes brighter than Type IIs. The assumed broad dispersion in peak magnitude for Type II SNe, coupled with their higher intrinsic rate and greater relative UV flux *at maximum* conspire to make the *HST*-HDF SNe

search more sensitive to Type II SNe compared to Type Ia SNe *at the magnitude-redshift combination of SNe 1997ff and 1997fg.*

On the basis of environment for SN 1997ff where the host galaxy is an elliptical, interpretation as a Type Ia is favored despite the overall statistical preference as shown in Fig. 17 for Type II SNe at this magnitude redshift combination.

For SN 1997fg the host galaxy is an irregular which does not provide an environmental restriction on SN type. Fig. 16 would suggest that interpretation as a Type II event is favored at about the 80% level relative to the statistical probability of this being a Type Ia.

6. Summary and Discussion

We have shown that deep imaging *HST* data is well suited to the detection and study of SNe at high redshift. The long term stability provided by *HST* allows for a straightforward quantification of completeness limits that remain high to $m_I \gtrsim 27$ for high redshift galaxy hosts in these data, and for which the dependence on host galaxy redshift is well quantified.

A search of two epochs of HDF data in the F814W filter is sensitive to SNe Ia and II to $z \sim 1.8$. We detected two supernovae, one of which is most probably a SNe Ia based primarily on its late type host galaxy; the other with a (spectroscopic) redshift of 0.952 for the host galaxy and $m_I \sim 26.0$ may be either a SN Ia or SN II event, but factoring in the early host galaxy type and relative detection rates developed in §5 statistically favors a Type II interpretation.

Our two SNe detections from a two epoch search of the HDF are consistent with general expectations for the cosmic rates of Type Ia and II events. These small number statistics do not yet support placing meaningful constraints on different cosmologies, or assumptions regarding Type Ia formation for which the parameter space of possible rates

at modest $z \sim 1 - 2$ is still relatively open. We have demonstrated with current technology a sensitivity to detecting SNe to $z \sim 1.8$ and note that with the much improved “discovery space” (product of area and efficiency) of the Advanced Camera for Surveys (to be installed on HST in 2000) in the $0.8 - 1.0 \mu$ range relative to WFPC2 that programs to return a statistically robust sample of both Type Ia and II events to $z \sim 2$ will be feasible.

We thank Andy Fruchter for numerous discussions related to data reductions of the HDF data; illuminating exchanges are also appreciated with Rodrigo Ibata. Discussions with Greg Aldering concerning the SFR were very enlightening as were conversations with Doug Leonard on the spectra of SNe II. Massimo Turatto kindly provided digital copies of their SN II light curve templates. Alberto Fernández-Soto and Ken Lanzetta kindly provided access to their data base on HDF galaxy redshifts and properties well in advance of publication and provided associated discussion. We thank Mark Dickinson for general discussion of the HDF and photometric redshift determinations. We thank Bob Williams for encouragement and for initiating the HDF observations. R.L.G. acknowledges the hospitality of the Astronomy and Astrophysics Department at UC Santa Cruz where much of this work was done, the ST ScI for a sabbatical leave, and support via GO-6473.01-95A. Calculations presented in this paper were performed at the National Energy Research Supercomputer Center; P.E.N. acknowledges support under DoE 76SF0098 and by the Director, Office of Computational and Technology Research of the U.S. DoE.

References

- Aldering, G., et al. 1998, IAU Circ. No. 7046.
- Cappellaro, E., Turatto, M., & Fernley, J. 1995, *IUE - ULDA Access Guide No. 6: Supernovae*, ESA, The Netherlands.
- Cappellaro, E., Turatto, M., Tsvetkov, D. Y., Bartunov, O. S., Pollas, C., Evans, R., & Hamuy, M. 1997, *A&A*, 322, 431.
- Cardelli, J. A., Clayton, G. C., & Mathis, J. S. 1989, *ApJ*, 345, 245.
- Cohen, J., Cowie, L., Hogg, D., Songaila, A., Blandford, R., Hu, E., & Snopbell, P. 1996, *ApJ*, 471, L5.
- Connolly, A. J., Szalay, A. S., Dickinson, M. E., SubbaRao, M. U., & Brunner, R. J. 1997, *ApJ*, 486, L11.
- Dahlen, T., & Fransson, C. 1998, astro-ph/9809379.
- Dickenson, M., et al. 1999, *ApJ*, in preparation.
- Fernández-Soto, A., Lanzetta, K. M., & Yahil, A. 1998, *ApJ*, in press.
- Flynn, C., Gould, A., & Bahcall, J. N. 1996, *ApJ*, 466, L55.
- Fomalont, E. B., Kellermann, K. I., Richards, E. A., Windhorst, R. A., & Patridge, R. B. 1997, *ApJ*, 475, L5.
- Garnavich, P., et al. 1998, *ApJ*, 493, L53.
- Gilliland, R. L., et al. 1995, *ApJ*, 447, 191.
- Gilliland, R. L., & Phillips, M. M. 1998, IAU Circ. No. 6810.

- Gronwall, C. 1998, astro-ph/9806240.
- Hamuy, M. 1999, private communication.
- Hamuy, M., Phillips, M. M., Suntzeff, N. B., Schommer, R. A., Maza, J., & Aviles, R. 1996a, AJ, 112, 2398.
- Hamuy, M., Phillips, M. M., Maza, J., Suntzeff, N. B., Schommer, R. A., & Aviles, R. 1996b, AJ, 112, 2391.
- Hatano, K., Branch, D., & Deaton, J. 1998, ApJ, 502, 177.
- Hauschildt, P. H., Shore, S. N., Schwarz, G., Baron, E., Starrfield, S., & Allard, F. 1997, ApJ, 490, 803.
- Hauschildt, P. H., Baron, E., & Allard, F. 1997, ApJ, 483, 390.
- Holtzman, J. A., et al. 1995, PASP, 107, 156.
- Kirshner, R., et al. 1993, ApJ, 415, 589.
- Kobayashi, C., Tsujimoto, T., Nomoto, K., Hachisu, I., & Kato, M. 1998, ApJ, 503, L155.
- Leibundgut, B. 1988, Ph.D. thesis, University of Basel.
- Lilly, S. J., Fèvere, O. L., Hammer, F., & Crampton, D. 1996, ApJ, 455, 108.
- Madau, P., Valle, M. D., & Panagia, N. 1998, MNRAS, 297, L17.
- Madau, P., Pozzetti, L., & Dickinson, M. 1998, ApJ, 498, 106.
- Miller, D., & Branch, D. 1990, AJ, 100, 530.
- Miralda-Escudé, J., & Rees, M. J. 1997, ApJ, 478, L57.
- Pain, R., et al. 1996, ApJ, 473, 356.

- Pain, R., et al. 1999, ApJ, in preparation.
- Patat, F., Barbon, R., Cappellaro, E., & Turatto, M. 1993, A&AS, 98, 195.
- Patat, F., Barbon, R., Cappellaro, E., & Turatto, M. 1994, A&A, 282, 731.
- Perlmutter, S., et al. 1997, ApJ, 483, 565.
- Perlmutter, S., et al. 1999, ApJ, in press.
- Phillips, A. C., Guzman, R., Gallego, J., Koo, D. C., Lowenthal, J. D., Vogt, N. P., Faber, S. M., & Illingworth, G. D. 1997, ApJ, 489, 543.
- Phillips, M. M. 1993, ApJ, 413, L105.
- Phillips, M. M., Lira, P., Suntzeff, N. B., Schommer, R. A., Hamuy, M., & Maza, J. 1999, AJ, submitted.
- Richards, E. A., Kellermann, K. I., Fomalont, E. B., Windhorst, R. A., & Partridge, R. B. 1998, AJ, 116, 1039.
- Riess, A., et al. 1998, AJ, 116, 1009.
- Riess, A. G., Press, W. H., & Kirshner, R. P. 1995, ApJ, 438, L17.
- Riess, A. G., Press, W. H., & Kirshner, R. P. 1996, ApJ, 473, 88.
- Rowan-Robinson, M., et al. 1997, MNRAS, 289, 490.
- Ruiz-Lapuente, P., & Canal, R. 1998, ApJ, 497, L57.
- Sadat, R., Blanchard, A., Guiderdone, B., & Silk, J. 1998, A&A, 331, L69.
- Sandage, A., Saha, A., Tammann, G., Labhardt, L., Panagia, N., & Macchetto, F. D. 1996, ApJ, 460, L15.

Sawicki, M., Lin, H., & Yee, H. 1997, *AJ*, 113, 1.

Schmidt, B. P., et al. 1994, *ApJ*, 432, 42.

Schmidt, B. P., et al. 1998, *ApJ*, 507, 46.

Stetson, P. B. 1987, *PASP*, 99, 191.

Suntzeff, N. B., Phillips, M. M., Covarrubias, R., Navarrete, M., Perez, J. J., Guerra, A.,
Acevedo, M. T., Doyle, L. R., Harrison, T., Kane, S., Long, K. S., Maza, J., Miller, S.,
Piatti, A., Claria, J. J., Ahumada, A. V., Pritzl, B., & Winkler, P. F. 1999, *AJ*, in press.

Treyer, M. A., Ellis, R. S., Milliard, B., Donas, J., & Bridges, T. J. 1998, *astro-ph/9806056*.

Williams, R. E., et al. 1996, *AJ*, 112, 1335.

Yungelson, L., & Livio, M. 1998, *ApJ*, 497, 168.

Fig. 1.— First and second epoch direct images of SN 1997ff in galaxy 4-403.0 are shown in the upper panels. The lower right panel shows the difference image (second minus first epoch) in which a point source residual at a magnitude of $m_I \sim 27.0$ corresponding to the supernova can be seen.

Fig. 2.— The first and second epoch direct images of SN 1997fg in galaxy 3-221.0, and the difference image showing the $m_I \sim 26.0$ point source corresponding to the supernova.

Fig. 3.— Direct and difference images over a wider area than in Figs 1 & 2 for both SN 1997ff and SN 1997fg.

Fig. 4.— Radial plots and associated Gaussian profile fits for (left panels) SN 1997ff and 1997fg, and (right panels) stars from the same CCD as the respective supernovae.

Fig. 5.— The daily magnitudes derived for each of SN 1997ff and 1997fg are overplotted on a Type Ia supernova light curve that has been properly shifted in magnitude and time dilated for the assumed redshift of the host galaxy. Time is with respect to maximum light in the B -band.

Fig. 6.— Light curves for Type Ia SNe derived for $z = 0.25$ (top) to $z = 1.75$ (bottom) in I-band apparent magnitudes for an event of average intrinsic brightness. A fiducial dashed line at $m_I = 27.3$ shows the $\sim 50\%$ completeness limit for $z = 1.2$ galaxies in our HDF data.

Fig. 7.— Expected number of SNe Ia events in the two epochs of the HDF data per unit redshift based on assuming a constant rate per unit volume with redshift (at the Pain *et al.* 1997 $z \sim 0.4$ value) and the assumed $\Omega_M = 0.28$, $\Omega_\Lambda = 0.72$, $h = 0.633$ cosmology.

Fig. 8.— (Upper) Apparent m_I magnitudes at peak plotted against redshift for the 5000 SNe Ia generated in our Monte Carlo simulation of an HDF search for an $\Omega_M = 0.28$, $\Omega_\Lambda =$

0.72, $h = 0.633$ cosmology. (Lower) Apparent m_I magnitudes at discovery plotted against redshift for the same simulation. The solid line shows for comparison the ridge line of input peak magnitudes.

Fig. 9.— The expected number of SNe Ia events in the two epochs of the HDF data per unit redshift are contrasted for three different cosmologies: *Solid line*: a cosmological constant dominated universe, *Dashed line*: an open, matter only universe, and *Dotted line*: a matter only, critical density universe.

Fig. 10.— Comparison of synthetic SNe II spectrum (solid curve) with a representative blackbody (dotted curve) matching the optical. The dashed curve shows the wavelength origin that F814W passes for a modest $z = 1.0$ redshift – for typical cases the UV flux is a small fraction of that predicted from common blackbody representations.

Fig. 11.— I-band magnitude comparison of representative blackbody (dashed line) and a spectrum synthesis model for a SNe II-P mid-plateau phase 40 days after outburst. At redshifts beyond $z \sim 0.8$ predicted magnitudes for Type II-P events drop rapidly in the spectrum synthesis model due to suppressed UV flux.

Fig. 12.— Representative light curves for Type II SNe at redshifts of 0.5, 0.75 and $z = 1.0$ (compare with Ia light curves in Fig. 6).

Fig. 13.— The difference in luminosity density arising from the assumed Madau, Pozzetti, & Dickinson (1998) $\Omega_M = 1.0$ and our assumed standard flat, but Λ dominated universe.

Fig. 14.— Expected number of SNe II-P events in the two epochs of HDF data per unit redshift based on assuming a constant rate (at $2.3 \times$ local – see text) per unit volume with redshift.

Fig. 15.— Same as for Fig. 12, but for SNe II-L.

Fig. 16.— A histogram of the discovery magnitudes given our simulations for the three types of SNe at a $z = 0.95$.

Fig. 17.— Same as for Fig. 16, but for a $z = 1.3$.

Table 1. First and Second Epoch Data Summary

Filter	Mean epoch (MJD)	Number Frames	Number Dithers	Total Exp. Time (s)	T_{exp}/frame (s)	Sky (e-/s)
F814W	50075.5594	58	10	123600	1100-3100	0.0445
F814W	50807.4587	36	17	63000	1600,1900	0.0448
F300W	50807.4819	18	17	27300	1100,1600	0.0038

Table 2. Comparison of PSF FWHM and Background Noise with V. 2 Drizzle Release

Filter	Chip	% diff. noise ^a	% diff. FWHM ^b	Mag. gain ^c
F300W	PC1	-21.8	-7.9	0.28
F300W	WF2	-6.9	+0.7	0.07
F300W	WF3	-9.3	-6.8	0.16
F300W	WF4	-1.1	-7.1	0.09
F814W	PC1	-6.0	-6.9	0.13
F814W	WF2	-5.4	-5.1	0.11
F814W	WF3	+0.4	0.0	-0.00
F814W	WF4	-1.4	-9.6	0.10

^aNoise levels were evaluated as the standard deviation of pixel values in the same regions of both reductions dominated by background and corrected for the effects of over-sampling (correlated noise), negative values reflect lower noise levels in the current reductions.

^bPSF widths were measured for an isolated bright star (or closest approximation in case of PC data) using the IRAF-imexamine task and a radial fit to report the enclosed energy statistic for width; negative values reflect sharper PSFs in these reductions.

^cExpected point-source limiting magnitude gain of new reductions (for original epoch only) as $2.5 \log_{10}(1 - \text{fractional noise} - \text{fractional FWHM difference})$.

Table 3. Top False Alarms in Control Experiments

Chip	Epoch	Type ^a	m_I	mag-err	sharp ^b	host
WF4	1	sim	27.853	0.367	-0.072	$m_I = 20.9$ galaxy
WF3	1	sim	27.860	0.235	-0.036	none
WF3	2	e-o	27.864	0.201	-0.187	$m_I = 21.4$ galaxy
WF4	1	e-o	27.895	0.230	-0.043	none
WF2	2	e-o	27.898	0.328	-0.168	$m_I = 21.4$ galaxy

^aType of control experiment, “e-o” stands for the even minus odd numbered frame epochs, and “sim” for the simulation of noise.

^bThe sharpness statistic reported by DAOPHOT, stellar sources should have values near zero.

Table 4. Top Potential SN Candidates

Chip	Epoch	m_I	mag-err	sharp	host, ID
WF3	2	26.014	0.093	0.115	$z=0.952$, SN 1997fg
WF4	2	26.957	0.079	-0.018	$z=1.32$, SN 1997ff
WF2	2	27.100	0.171	0.108	$m_I = 18.7$ star
WF3	1	27.351	0.284	0.027	$z=0.52$, 3-404.2
WF2	1	27.453	0.262	-0.043	$m_I = 18.7$ star
WF3	2	27.512	0.191	-0.153	$m_I = 18.9$ star
WF3	1	27.642	0.297	0.114	$m_I = 18.9$ star

Table 5. Completeness Limits (%)

Magnitude	$z = 0.2^a$	$z = 0.7$	$z = 1.2$	$z = 1.7$
23.7	72	90	98	100
24.9	53	83	98	100
25.2	47	80	97	100
25.5	41	76	96	100
25.8	28	72	92	100
26.1	22	62	89	100
26.4	13	56	84	100
26.7	9	47	78	99
27.0	8	38	72	94
27.3	5	27	56	77
27.6	2	10	26	42
27.9	0	3	8	7

^aGalaxy redshift range, to which artificial stars were added as described in text, of listed central value ± 0.2 .

Table 6. Time Resolved Magnitudes

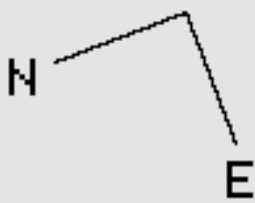
Date (UT) Dec. 1997	SN 1997ff	SN 1997fg
23.83	26.97 ± 0.15	25.90 ± 0.06
25.78	27.12 ± 0.15	26.16 ± 0.08
26.74	26.95 ± 0.13	26.03 ± 0.06
Mean ^a	27.00 ± 0.08	26.02 ± 0.04

^aThe mean magnitude follows from PSF fit analysis over the full data set.

1ST EPOCH

2ND EPOCH

1"



DIFFERENCE

SN 1997FF

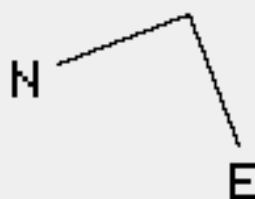
1ST EPOCH



2ND EPOCH



1"

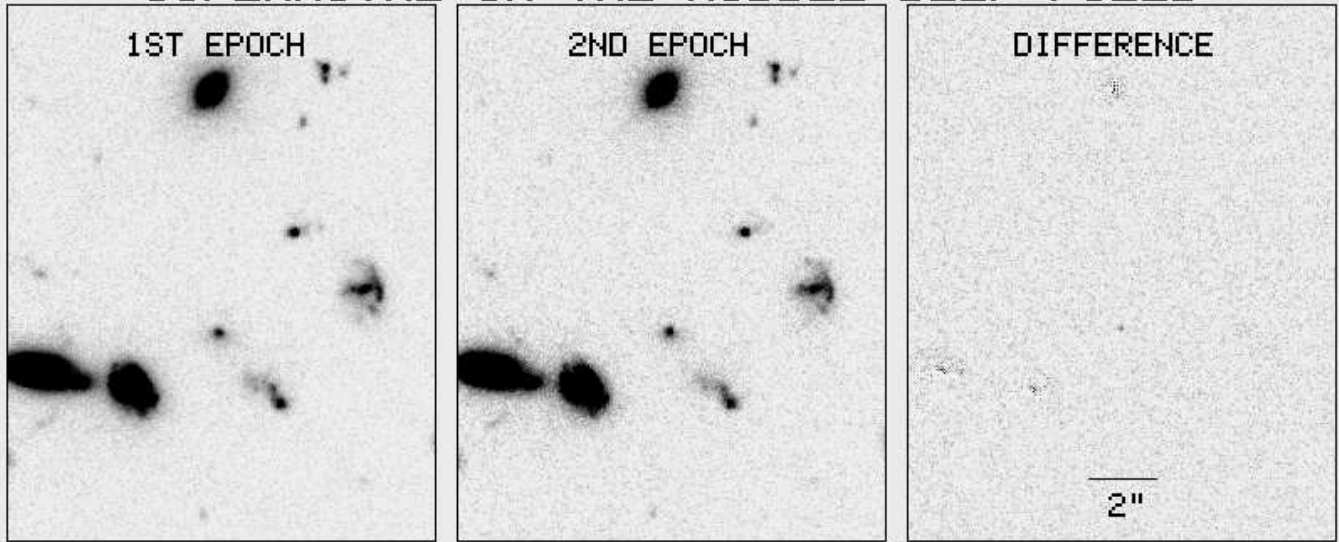


SN 1997FG

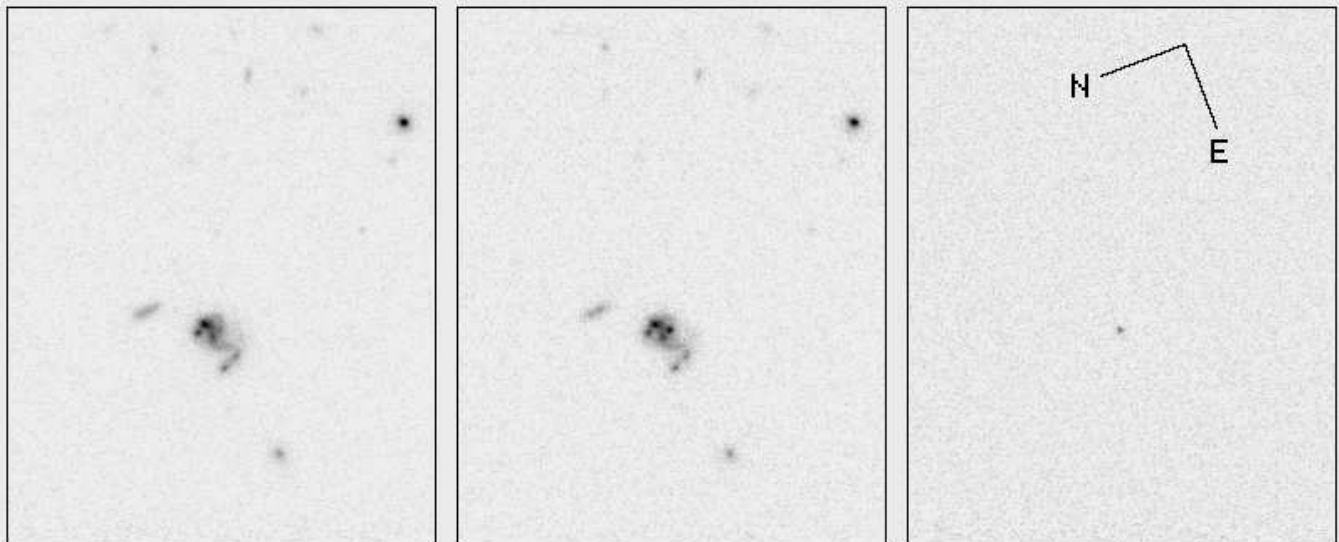
DIFFERENCE



SUPERNOVAE IN THE HUBBLE DEEP FIELD



SN 1997FF



SN 1997FG

